Stratigraphic variation of transport properties and overpressure development in the Western Foothills, Taiwan

Wataru Tanikawa[1]*

Toshihiko Shimamoto[2]

Sheng-Kuen Wey[3]

Ching-Weei Lin[4]

Wen-Chi Lai[4]

1 Kochi Institute for Core Sample Research, Japan Agency for Marine-Earth Science and Technology, Nankoku, Japan

2 Department of Earth and Planetary Systems Science, Graduate School of Science, Hiroshima University, Higashi-Hiroshima, Japan

3 Chinese Petroleum Corporation, Miaoli, Taiwan

4 Disaster Prevention Research Center, National Cheng Kung University, Tainan, Taiwan

*Corresponding author

Address: Kochi Institute for Core Sample Research, Japan Agency for

Marine-Earth Science and Technology, Nankoku 783-8502, Japan
Tel: +81-88-878-2203; fax: +81-88-878-2192
E-mail: tanikawa@jamstec.go.jp

Abstract

Overpressure, fluid pressure higher than hydrostatic pressure, has developed below the middle Miocene formations in the north-central Western Foothills of Taiwan. To study the mechanism by which overpressure is generated and maintained in the Taiwan oil fields, we estimated the fluid pressure history and overpressure distribution by using a one-dimensional basin model incorporating laboratory-approximated hydraulic parameters. Transport properties of outcropping sedimentary rocks were measured at effective pressures of 5 to 200 MPa. All parameters showed apparent stratigraphic variation, decreasing with increasing burial depth. Permeability showed the strongest sensitivity to depth, decreasing by 6 orders of magnitude to 10^{-20} m^2 at the bottom of the basin. A critical sealing layer was not identified in the geologic column. The basin model incorporates overburden loading due to sediment accumulation, aquathermal expansion of water, the dehydration reaction of expandable clay to nonexpandable clay, and oil generation. Predicted overpressure was generated dramatically from 3 Ma, when the accumulation rate increased rapidly as a result of tectonic collisions in the area. If we assume a fluid influx from the bottom of the basin, the predicted overpressure is consistent with the observed overpressure, implying that continuous inflow from depth, possibly along the décollement or normal faults, may be the main cause of overpressure generation in this area. Stratigraphic variation of transport properties, which decrease with depth, also influences overpressure trends in the Western Foothills, where overpressure is generated only in deeper horizons. The clay mineral distribution estimated by a kinetic smectite–illite dehydration model is consistent with the observed mineralogical data.

1. Introduction

Overpressure, which is fluid pressure higher than hydrostatic pressure, is observed in numerous oil fields and thick sedimentary basin sequences at depth [Hunt, 1990; Law and Spencer, 1998]. Some basins (e.g., the Gulf Coast, Uinta Basin, Sacramento Basin, and Scotian Shelf in North America) [Bethke, 1986; Bredehoeft et al., 1994; McPherson and Garven, 1999] show over 20 MPa of elevated excess pressure, so that pressure in a part of the overpressured sections approaches the lithostatic level. Overpressure affects sediment consolidation [Hart et al., 1995] as well as groundwater circulation patterns [Harrison and Summa, 1991] and oil and gas generation and migration mechanisms [McPherson and Bredehoeft, 2001]. It also influences thrust fault strength and slip behavior, and the updip limit of the seismogenic zone [e.g., Moore and Saffer, 2001]. Prediction of the fluid pressure distribution at depth has useful engineering applications for prediction of oil and gas penetration. Numerous possible mechanisms of overpressure generation and maintenance in thick sedimentary basins have been described theoretically in recent decades [Bethke and Corbet, 1988; Luo and Vasseur, 1992; Osborn and Swarbrick, 1997; Wangen, 2001]. Mechanical compaction from overburden loading is one of the main mechanisms of overpressure generation. Thermal expansion of water, dehydration of clay minerals, hydrocarbon generation from source rocks, and inflow of water from depth are other probable mechanisms. The primary mechanism for the generation and maintenance of overpressure may differ depending on the local geological setting and conditions. Hydrocarbon generation is the most likely cause of overpressure in the Uinta Basin [McPherson and Garven, 1999], while sediment compaction is the main driving force in the Pleistocene Gulf Coast Basin [Hart et al., 1995]. The dominant hydraulic properties affecting the generation of excess fluid pressure in thick sedimentary basins are permeability and porosity and the poroelastic properties specific storage and loading efficiency (or Skempton's coefficient) [e.g., Wang, 2000]. Permeability and porosity show stratigraphic variation in sedimentary basins according to the lithology and the degree of mechanical and time- and temperature-dependent consolidation [Dutton and Diggs, 1992; Ingebritsen and Manning, 1999], causing these parameters to decrease with burial depth in sedimentary basins. Specific storage and loading efficiency are not as well documented as permeability and porosity, even though they are also important parameters controlling hydraulic transport in porous media. Bethke and Corbet [1988] suggested that the nonlinear manner with which permeability and specific storage change with depth affects the behavior of overpressure generation in sedimentary basins.

Despite the importance of understanding the origin and generation of overpressure, few studies have incorporated detailed transport property data into numerical models [e.g., Bredehoeft et al., 1994]. It is also important to analyze quantitatively the relative importance of the various mechanisms that generate pore pressure. For our study, we selected the Western Foothills, Taiwan, as the case study area. In the north-central Western Foothills, where several of the major oil fields of Taiwan are found, high fluid pressures exceeding the hydrostatic gradient by 10 MPa (fluid:solid pressure ratio, λ, is about 0.7) are observed at depth in several wells [Suppe and Wittke, 1977; Namson, 1982; Davis et al., 1983]. Suppe and Wittke [1977] suggested on the basis of the observed overpressure data that the fluid pressure distribution in the Western Foothills is controlled by stratigraphy rather than by burial depth. However, hydraulic data for the sedimentary basin sequence at this site have never been published, making it difficult to demonstrate the cause of the overpressure at depth in the Western Foothills. The stratigraphy and tectonic structure of the Western Foothills have been described in detail

[Namson, 1982], and geochemical analyses of petroleum generation have revealed the kinetic parameters of the source rocks of this oil field [Chiu and Chou, 1991; Chiu et al., 1996], providing useful data for application to modeling fluid pressures in the sedimentary basin sequence. Although Oung [2000] previously carried out a basin analysis in a Tertiary sedimentary basin offshore of Taiwan, he focused mostly on hydrocarbon generation, which is controlled by time- and temperature-dependent reactions.

In this study, we measured the hydraulic properties of sedimentary rocks from the Western Foothills under high confining pressure in laboratory tests, using samples collected from representative stratigraphic horizons. Then we used the data in a numerical model to estimate the fluid pressure distribution. Finally, we compared the predictions of our numerical model with observed borehole data. As we lacked information on fluid sources and the amount of fluid influx, we roughly evaluated how an influx of fluid would influence overpressure generation. In addition, we used a kinetic reaction model to predict the dehydration reaction of smectite to illite, because this geochemical process may contribute to overpressure generation in a thick sedimentary basin sequence.

2. Geological setting and overpressure data

Taiwan is on the boundary between the Philippine Sea and Eurasian tectonic plates (Fig. 1a). The Philippine Sea plate is subducting beneath the Eurasian plate along the Manila Trench, and the two plates are converging at an estimated rate of about 8 cm/year in a northwest–southeast direction [Yu et al., 1999]. Taiwan can be divided into several regions of distinct geology and physiographic character, which trend mainly north–northeast: from west to east, the Coastal Plain, the Western Foothills, the Hsueshan Range, the Central Range, and the Coastal Range. A structural front, the Shuichangliu fault, separates the nonmetamorphosed clastic Neogene sediments of the Western Foothills from the submetamorphic argillaceous Neogene and Paleogene rocks of the Central Range (Fig. 1b).

A thick sedimentary basin sequence has accumulated in the Western Foothills region as a result of the oblique collision between the Luzon Arc and the Chinese continental margin [Teng, 1990]. The major structure of the Western Foothills is a system of NNE-SSW-trending folds and west-vergent thrust faults. The sedimentary sequence comprises mainly littoral to shallow marine Oligocene to Neogene rocks. The oil fields of Taiwan are in the north-central Western Foothills. The oil and gas fields are beneath the N-S-trending anticlines (Fig. 1b, 1c). The Chuhuangkeng oil field, the largest and oldest oil field in Taiwan, is about 14 km southeast of Miaoli city. In this area, geophysical and geochemical studies performed during oil and gas exploration provide abundant pore pressure data. The Chinese Petroleum Corporation has performed both in situ measurements during shut-in borehole tests and indirect sonic log measurements of fluid pressure in many of the oil fields in Taiwan [Suppe and Wittke, 1977; Namson, 1982; Davis et al., 1983]. Suppe and Wittke [1977] summarize the relationship among pore pressure, stratigraphy, and depth in the Western Foothills. (The stratigraphy of the north-central Western Foothills is summarized in Table 1, after Teng [1990] and Lee [2000].) Their data show that fluid pressure is very close to the hydrostatic gradient in shallower horizons, but overpressure has developed in the Early Miocene sedimentary rocks at 2 to 4 km depth. The overpressure increases linearly with depth at fluid pressure gradients corresponding to λ = 0.7. The transition zone to overpressure is located between the Talu Shale and the Piling Shale, and the transition zone is mostly within the Chuhuangkeng Formation (Table 1). They concluded that overpressure is stratigraphically controlled and that an effective permeability seal might be present in the vicinity of the Chuhuangkeng Formation.

All formations of the sedimentary sequence, from the Late Oligocene Wuchihshan Formation to the Early Pleistocene Toukoshan Formation, were deposited in succession and they include no unconformities (Table 1). The stratigraphy can be divided into two major tectonostratigraphic units. The older sequence consists of preorogenic sediments from the stable Chinese continental margin, and the younger consists of orogenic sediments that reflect the collision and deformation of the Chinese continental shelf and the development of mountainous topography in this region. This stratigraphic transition occurred at the beginning of the Pliocene (about 5 Ma), when the Luzon arc and the Chinese continent began to collide and the northern tip of the arc began to encroach on the continental shelf as an accretionary wedge that grew above sea level. The tectonic changes resulting from the collision affected the sedimentation rate in the Western Foothills region as well. As the arc–continent collision progressed, the mountains of the Central Range uplifted more rapidly, shedding voluminous sediments into foreland basins (in the area of the Western Foothills). The sedimentation rate in the Western Foothills region, based on the accumulated sediment thickness versus age curve (Fig. 2; Lee [2000]), changed from 20 m/My before 3 Ma to a maximum of about 1500 m/My from 3 to 0.8 Ma. The surface folding probably occurred at about 0.5 Ma, after or during deposition of the Toukoshan Formation [Mouthereau and Lacombe, 2006]. The present surface in the study area is eroding or in a "steady state" condition, in which sediment accumulation and erosion rates are in balance. The current erosion rate in this area is very low [Dadson et al., 2003], though both erosion and loading may continue in several parts of the Western Foothills.

The Tertiary sediments in the north-central Western Foothills have been tectonically deformed, but active thrusting and folding has been confined to the shallow sedimentary rocks above the pre-Tertiary basement. The Chuhuangkeng anticline developed in the area is interpreted as a detachment fold (Fig. 1c). These thrust and anticline suggest the existence of a weak décollement at the base of the Upper Oligocene Wuchihshan Formation (Fig.

1c). This active décollement lies several kilometers below the top of the overpressured sequence. Recently acquired seismic data have also revealed that normal faults are developed within the pre-Tertiary basement, and some of the Paleogene normal faults have been reactivated as strike-skip faults [Mouthereau and Lacombe, 2006].

3. Experimental apparatus and measurement

We collected samples from outcrops of all Late Oligocene to Pleistocene formations in the Tungshih area of the Western Foothills for laboratory experiments (Fig. 1b). Samples of the Pliocene Cholan and the Pleistocene Toukoshan formations were collected in the central part of the Western Foothills, as these formations do not show characteristic differences between the north-central and central Western Foothills.

All samples for laboratory tests of hydraulic properties were cored and polished to cylindrical shapes. Then, the samples were dried at 80 °C in an oven for a week to eliminate pore water without removing structural water adsorbed to clay mineral surfaces. The specimens were 5 to 40 mm long and

20 mm in diameter. All experiments were performed in an intravessel oil pressure apparatus at Kyoto University at room temperature under uniform (isostatic) confining pressure. All parameters were measured by using nitrogen gas as the pore fluid, which enabled us to measure them more easily and quickly.

3-1. Permeability measurement

Permeability was measured by the steady-state gas flow method, with nitrogen gas as the pore fluid. A differential pore pressure was applied across the sample, and the volume of gas flowing though it per unit time was measured. Because a compressible gas was used as the pore fluid, the equation for evaluating the (intrinsic) gas permeability k_{gas} is expressed as follows [Scheidegger, 1974]:

$$\frac{Q}{A}=\frac{k_{gas}}{\mu L}\frac{\left(P_{up}\right)^2-\left(P_{down}\right)^2}{2P_{down}}, \tag{1}$$

where Q is the volume of fluid measured per unit time, A is the cross-sectional area of the sample, μ is the viscosity of the pore fluid, L is the sample length, and P_{up} and P_{down} are the pore pressure at the upper and lower ends of the specimen, respectively. In our apparatus, P_{up} was kept constant at a value between 0.2 and 2 MPa using a gas regulator, and the gas flow rate was monitored downstream of the samples with a commercial gas flow meter. Fluid flowing out of the specimen at the downstream end was released to atmospheric pressure, and P_{down} was assumed to have a constant value of 0.1 MPa.

The Klinkenberg effect [Klinkenberg, 1941], which enhances gas permeability, may cause significant error between gas and water permeabilities, especially at low pore pressure and low permeability. Therefore, the measured gas permeability was transformed to water permeability by using the Klinkenberg equation. The difference between gas and water permeabilities due to the Klinkenberg effect is expressed by the following relationship:

$$k_{gas} = k\left(1 + \frac{b}{\left(P_{up} + P_{down}\right)/2}\right), \qquad (2)$$

where k is the (intrinsic) permeability to water and b is the Klinkenberg factor, which depends on the pore structure of the medium and temperature of a given gas. In our experiments, gas permeability was measured four or five times at differential pore pressures ranging from 0.1 to 2.0 MPa at the same confining pressure, and the resulting values were plotted against the inverse of the average pore pressure (Fig. 3). Then, we determined *k* and *b* on the basis of the linear relationship described by equation (2). Permeabilities of most of the sedimentary rocks tested satisfied the Klinkenberg equation, as indicated by the linearity of the results.

3-2. Porosity measurement

Porosity change in response to confining pressure changes was determined by the gas expansion method [Scheidegger, 1974]. In this method, the volume of the gas contained in pore spaces of the rock sample is directly measured, and pore volume and porosity are evaluated by using the isothermal (Boyle-Mariotte) gas equations. The pore pressure change under undrained conditions is measured at each confining pressure step, and the change in pore volume is evaluated by using the following equation:

$$P_0 V_{p0} = P_1 V_{p1} = \cdots = P_i V_{pi} = P_{i+1} V_{p(i+1)}, \quad (3)$$

where P_0 is the initial pore pressure at the initial total pore volume V_{p0} (the pore volume of the sample and the system pore volume) and P_1 is the equilibrium pore pressure, corresponding to the total pore volume V_{p1} at the first confining pressure step. Assuming that the entire volume change represents the pore volume change in the specimen (i.e., that the grains and system volume are relatively incompressible in comparison with the compressibility of the pores of the specimens), we calculated pore volume and porosity.

3-3. Measurement of specific storage and Skempton's coefficient

When fluid compression is considered, and assuming that the rock grains are much less compressible than pore spaces (e.g., compressibility of mica is 1.2×10^{-11} Pa^{-1}, independent of pressure [Birch, 1966]), specific storage Ss can be evaluated from the drained pore compressibility β_{Φ} and pore fluid compressibility β_f as follows:

$$Ss = \beta_{\phi} + \Phi\beta_f \,, \tag{4}$$

where Φ is porosity.

The drained pore compressibility is calculated as follows:

$$\beta_{\Phi} = -\frac{1}{V_p}\frac{\partial V_p}{\partial Pc}\bigg|_{P=0} = -\frac{1}{1-\Phi}\frac{\partial \Phi}{\partial Pc}\bigg|_{P=0} , \qquad (5)$$

where V_p is pore volume, Pc is confining pressure, and P is pore pressure. Even though pore pressure increases with the effective pressure during porosity measurements, the pore pressure change is extremely small compared with the confining pressure change (in our test, the pore pressure change was less than 0.01 MPa for a step change in confining pressure of 10 MPa). We assumed that the condition of the sample was "drained" when pore pressure was constant. Therefore, we could calculate the drained pore compressibility from the results of the porosity test by using equation (5). The derivative of porosity with respect to confining pressure, $\partial\Phi/\partial Pc$, was interpolated between two median derivative values [Wibberley, 2002]. Fluid compressibility β_f was assumed to be constant at 4.4×10^{-10} Pa^{-1} in this study.

The undrained pore pressure buildup coefficient, or Skempton's coefficient B, is defined as

$$B = \frac{\partial P}{\partial Pc}\bigg|_{m_f=0} = \frac{\beta_{\Phi}}{\beta_{\Phi} + \Phi\beta_f}, \qquad (6)$$

where m_f is the fluid mass content in porous materials. Equation (6) is a simplified equation that assumes that both unjacketed bulk compressibility and unjacketed pore compressibility are negligible. Skempton's coefficient can also be expressed in terms of porosity and drained pore compressibility [Green and Wang, 1986]. In the simplest case of Terzaghi's [1925] consolidation model, in which the pore fluid is incompressible ($\beta_f = 0$), B becomes 1. In this study, we used equation (6) to estimate Skempton's coefficient B from the drained pore compressibility β_Φ, which we also used with equation (4) to estimate specific storage Ss.

4. Experimental results: transport property measurements

4-1. Permeability

Cyclic effective pressure tests were performed on all specimens. Confining pressure was first increased from 0 to 200 MPa (or up to the confining pressure at which permeability reached its technical limitation; $k_{gas} = 10^{-19}$ m^2), and then decreased to 5 MPa. The permeability of the specimen was measured at various confining pressure steps. Gas flow rates achieved stable values within 10 minutes after the change of confining pressure and pore pressure, and a time dependence of permeability was not clearly observed during the experiments.

In the pressure cycling tests on sandstones and siltstones, initial permeability at 5 MPa ranged from 10^{-14} to 10^{-17} m^2, and permeability decreased as effective pressure increased (Fig. 4). The pressure sensitivity of permeability varied among specimens and decreased as effective pressure increased. The permeable Shangfuchi Sandstone (sample 4B2, the sampling location is the circled number 4 in Fig. 1b) and Kuanyinshan Sandstone (samples 7A2, and 7A3, the sampling location is the number 7) showed low sensitivity to effective pressure, and permeability decreased by less than 1 order of magnitude from the initial permeability even at the maximum effective pressure. In other samples, permeability was decreased by 2 to 4 orders of magnitude at the maximum effective pressure. The permeability change was relatively small during unloading, and permeability did not fully recover its initial value even at the lowest effective pressure. This common behavior implies that permeability records the effective pressure history.

The cyclic pressure behavior of siltstones (Fig. 4b) was similar to that of sandstones, though several siltstone samples (18C2, 18C3, and Cholan Fm) showed stronger sensitivity to effective pressure than the sandstones. In general, the permeability of sandstone was 2 to 3 orders of magnitude larger than that of siltstone in the same unit (e.g., in the Cholan Formation).

4-2. Porosity

In sandstone, initial porosity ranged between about 5% and 20%, and porosity decreased as effective pressure increased, though only by 1% to 5% at the maximum effective pressure (Fig. 5a). The porosity change became less as effective pressure increased. As effective pressure decreased, porosity increased but did not recover its initial value, similar to the behavior of permeability. The pore volume reduction with the step increase of confining pressure ceased within 30 minutes, and further compaction was not observed under same confining pressure, suggesting that the time-dependence of porosity changes during the tests was negligible. In less porous rocks (porosity less than 5%), mostly Early Miocene and Late

Oligocene sedimentary rocks, porosity changes were extremely small, whereas in more porous rocks, porosity showed larger pressure sensitivity. Porosity changes did not differ significantly between sandstones and siltstones.

4-3. Specific storage

First, drained compressibility values, necessary for the estimation of specific storage, were estimated from the porosity data (Fig. 5a). Pore compressibility showed the same pressure sensitivity as porosity, and compressibility during loading was generally larger than that during unloading in the same specimen. Initially, specific storage ranged from 2×10^{-9} to 5×10^{-10} Pa^{-1}; it decreased rapidly by 1 order of magnitude with increasing effective pressure, and then approached a stable value (Fig. 5b). The pressure sensitivity of specific storage also decreased as effective pressure increased. Even though porosity differed greatly among specimens, the specific storage reduction curves were quite similar. Specific storage of most samples decreased to nearly 10^{-10} Pa^{-1} at high confining pressure.

Specific storage of some less porous samples decreased to less than 10^{-10} Pa^{-1} at high confining pressure.

4-4. Skempton's coefficient

Skempton's coefficient was also evaluated from the drained pore compressibility values estimated from the porosity measurements, using only the loading-path porosity data. Initial values of Skempton's coefficient were close to 1 in all samples, and the values decreased to 0.5–0.7 at maximum effective pressure (Fig. 5c). In both sandstone and siltstone samples, Skempton's coefficient decreased linearly with increasing effective pressure, but the slope of the line differed among samples. In sandstones, Skempton's coefficient was more sensitive to effective pressure changes than in siltstones.

4-5. Stratigraphic variation of transport properties

By plotting the hydraulic properties of the rocks from the Taiwan oil field, determined in the laboratory, against effective pressures equivalent to the previous maximum burial depth of the specimens to approximate in situ values, we estimated the stratigraphic variation of the transport properties of the rocks (Fig. 6) under hydrostatic pore pressure. The stratigraphic plot showed that permeability decreased as the depth of the stratigraphic horizon increased (Fig. 6a). In the uppermost horizon, permeability was 10^{-14} m^2, but it was less than 10^{-20} m^2 in Early Miocene rocks. Although a sealing layer could not be clearly identified in the column, permeability values in the Chinshui shale were more than 1 order of magnitude smaller than those in adjoining units. A large permeability gap, a difference of nearly 2 orders of magnitude, was also recognized between the Kuanyinshan Formation and the Talu Shale. Permeability in the Chuhuangkeng Formation was small, but it was not a sealing layer because no marked difference in permeability was recognized between the Chuhuangkeng Formation and its adjacent units, the Peiliao Sandstone and the Piling Shale. A log-linear plot using the minimum permeability values of each stratigraphic unit showed a linear trend, and permeability and effective pressure were related as follows:

$$k = k_0 \exp(-\gamma Pe), \tag{7}$$

where k_0 is the permeability at effective pressure Pe = 0 MPa and γ is the pressure sensitivity constant of permeability. This equation has the same form as that of David et al. [1994]. A large value of the sensitivity constant γ indicates that the loss of permeability becomes larger as effective pressure is increased. For $k_0 = 10^{-14}$ m^2, suitable values of the constant γ are from 0.12 to 0.18 MPa^{-1}.

At 50 to 80 MPa of effective pressure, corresponding stratigraphically to the Kueichulin to Peiliao formations, porosity data show a wide scatter (Fig. 6b). However, porosity decreased with depth when the lowest measured porosity values of each stratigraphic unit were selected. Porosity in the uppermost horizons was about 20%, and it decreased to 3% in the lowest horizon. The empirical relationship between porosity and effective pressure is described by Athy's law [1930]:

$$\Phi = \Phi_0 \exp\left(-\frac{\alpha}{\rho_e g} Pe\right), \qquad (8)$$

where Φ_0 is the initial porosity at 0 MPa of effective pressure and α is the compaction constant. ρ_e is the effective density, which is the difference between the bulk density of the sedimentary rocks ρ_s and water density ρ_w, and g is gravitational acceleration. If the initial porosity is assumed to be

60%, a value often used for unconsolidated soils, then the experimental data can be fitted for values of α from 4×10^{-4} to 8×10^{-4} MPa^{-1} (Fig. 6b).

In the shallowest horizon, specific storage was around 10^{-9} Pa^{-1}, and it decreased linearly with depth in a log-linear plot (Fig. 6c). Specific storage decreased to less than 10^{-10} Pa^{-1} in the deepest horizon; thus, its pressure sensitivity was quite small compared with that of permeability. By combining the differential form of Athy's law in equation (8) with equation (4), the following relationship between specific storage and porosity is obtained [Bethke and Corbet, 1988]:

$$Ss = \left(\frac{\alpha}{(1-\Phi)\rho_e g} + \beta_f \right)\Phi . \quad (9)$$

Therefore, specific storage is also a function of effective pressure. We compared the experimentally obtained values of specific storage with those predicted by equation (9) for the values of α that fitted the porosity data and found that the measured specific storage values were about 1 order of magnitude less than those predicted by equation (9).

Skempton's coefficient B decreased linearly from 1 to 0.7 as effective pressure increased from 0 to 100 MPa (Fig. 6d). This relationship can be stated as

$$B = 1 - \zeta \times Pe, \tag{10}$$

where ζ is the constant of effective pressure sensitivity relative to B. Our data were well-fitted by this equation for ζ in the range of 0.002 to 0.004 MPa^{-1}. By combining equation (6) and Athy's law (equation 8), Skempton's coefficient can also be expressed as a function of effective pressure. According to this approximation curve, B remains near 1 as effective pressure increases even when the compaction constant α is changed, a result that is much different from our experimental result.

5. Numerical modeling of overpressure generation

5-1. Sedimentation model and its relevant hydraulic parameters

To evaluate the overpressure generation history of the oil field, we applied a one-dimensional sedimentation model modified from Bethke and Corbet [1988], Luo and Vasseur [1992], Furbish [1997], and Wangen [2001], and based on the work of Gibson [1958]. The tectonic deformation history of the Western Foothills from Late Oligocene to the present is complicated, making it difficult to construct a multi-dimensional model. As our focus was the influence of stratigraphic variation of transport properties on overpressure generation, we employed a simplified one-dimensional model. In our model, sediments accumulate on an impermeable (basement flux q = 0 m/s or permeability k = 0 m^2) or permeable basement (q > 0 m/s) at vertical coordinate z = 0 m, and the sediment surface (z = $l(t)$) rises as sediment accumulates (Fig. 7). The model equation can be written as follows (see Appendix A):

$$\frac{\Delta P}{dt} = \frac{1}{Ss}\frac{\partial}{\partial z}\left(\frac{k}{\mu}\frac{\partial}{\partial z}P\right) + B\frac{\Delta Pc}{dt} + \frac{1}{Ss}\left(\Phi\alpha_f\frac{\Delta T}{dt} + Q_{deh} + Q_{oil}\right). \qquad (11)$$

The initial and boundary conditions, which assume no influx of fluid from the basement, are

$$\begin{aligned} &l = 0 && t = 0 \\ &P(l,t) = 0 && t > 0 \\ &\left.\frac{\partial P}{\partial z}\right|_{z=0} = 0 && t > 0 \end{aligned}.$$

α_f is the thermal expansibility of the fluid, and the thermal expansibility of the grain matrix is assumed to be 0. T is temperature, Q_{deh} represents the pore pressure generation term for dehydration of clay minerals, and Q_{oil} is the pore pressure generation term for hydrocarbon generation. Equation (11) is based on Darcy's law, the mass conservation law for both the fluid and the grain matrix, and Terzaghi's effective pressure law ($Pe = Pc - \tau P$), where the Biot-Williams coefficient τ is assumed to be 1. Equation (11) takes into account overburden loading with disequilibrium compaction, aquathermal pressuring, dehydration of clays, and hydrocarbon generation. $\Delta Pc/dt$ is equivalent to the burial rate ω. $\Delta T/dt$ is related to both the geothermal gradient and the burial rate. The transport properties permeability, specific storage, and Skempton's coefficient in equation (11) vary with depth, as we showed in the laboratory tests. All transport property values used in the model were based on the laboratory results. Equations (7), (8), and (10), which describe the effective pressure sensitivities of permeability, porosity, and Skempton's coefficient, were also used for the numerical simulation. We used a curve fitted to the specific storage values (shown in Figure 6c) for the simulation. The other parameter values used in the numerical analysis are listed in Table 2. The transport properties permeability, specific storage, and Skempton's coefficients depend on both depth (or vertical loading) and pore fluid pressure. Therefore, all parameters are described as a function of effective pressure, which changes with confining pressure and pore pressure. The sedimentation history, one of the most difficult to determine parameters required for basin analysis, was based on the sediment accumulation history reported by Lee [2000] (Fig. 2). Our numerical analysis starts from the deposition of the Shuichangliu Formation at 30 Ma, after which sediments accumulated continuously. Present erosion rates of 1 to 4 km/My in the northern Western Foothills have been reported by Dadson et al. [2003], but the temporal change in the exhumation rate is not known. Therefore, we assumed that no erosion occurred after sedimentation ceased at 0.8 Ma, which is when, according to our model, generation of excess fluid pressure ceased, though it is probable that deposition is continuing in several areas of the Western Foothills. We assumed the geothermal gradient at this site to be 30 °C/km on the basis of measured data reported by Suppe and Wittke (1977).

5-2. Dehydration submodel (smectite = illite + water)

The dehydration submodel associated with overpressure generation presented here is based on the work of Pytte and Reynolds [1988], Audet [1995], and Wangen [2001]. The dehydration model of Pytte and Reynolds

[1988] reasonably explains the field evidence for a smectite to illite transition. The amount of water derived from dehydration of smectite is calculated from the loss of smectite according to the following chemical reaction:

$$[\text{smectite}] = [\text{illite}] + n[\text{H}_2 0], \qquad (12),$$

which indicates that n moles of water are released when 1 mole of smectite is converted to 1 mole of illite. The kinetic model of the illitization of smectite is

$$\frac{\partial \Phi_{sm}}{\partial t} = -A_{sm}\exp\left(-\frac{E_{sm}}{RT}\right)\times\left(\Phi_{sm}\right)^{\alpha}\times\left[74.2\exp\left(-\frac{2490}{T}\right)\right]^{\beta}, \qquad (13)$$

where Φ_{sm} is the volume fraction of smectite (the mole fraction or concentration of smectite is often used instead of the volume fraction). The constant A_{sm} is the pre-exponential constant for the smectite transition, E_{sm} is the activation energy required for the reaction, and R is the gas constant. A fifth-order kinetic expression was used for the basin analysis: fourth-order with respect to the smectite fraction, $\alpha = 4$, and first-order with respect to the potassium fraction, $\beta = 1$ [Elliott et al., 1991]. Φ_{sm} can be obtained by solving differential equation (13). In our model, the temperature that smectite experiences, T, is described as a function of depth and time, based on the sedimentation history (Figure 2) and a geothermal gradient of 30 °C/km .

The Q_{deh} term in equation (11) is calculated as follows:

$$Q_{deh} = -n \frac{V_f}{V_{sm}} \frac{\partial \Phi_{sm}}{\partial t}, \quad (14)$$

where V_f and V_{sm} are the molar volumes of water and smectite, respectively. The parameter values used for the numerical model are shown in Table 2.

5-3. Hydrocarbon generation submodel

A submodel for the transformation of kerogen to oil is also applied in our model [Wangen, 2001]. In this submodel, the secondary oil to gas cracking and kerogen to gas reactions are ignored, the single-phase flow of water is assumed, and oil and gas flows are neglected. Therefore, overpressure can be caused by a difference of density between kerogen and oil. By applying first-order kinetics with an Arrhenius-type parallel reaction equation to the hydrocarbon reaction model, the fluid pressure generation factor due to oil generation Q_{oil} is calculated as follows:

$$Q_{oil} = \left(\frac{\rho_k}{\rho_o} - 1 \right) \sum_{i=1}^{n} A_{ki} \exp\left(-\frac{E_{ki}}{RT} \right) x_i \Phi_k \,, \qquad (15)$$

where i indicates the i^{th} reaction, x_i is the initial fraction of reactant of the i^{th} reaction, Φ_k is the volume fraction of the total kerogen component, ρ_k/ρ_o is the density ratio of kerogen to oil, and A_{ki} and E_{ki} are the pre-exponential constant and the activation energy of the kerogen reaction corresponding to the i^{th} reaction, respectively.

The kinetic properties of kerogen from the western Taiwan Basin are known [Chiu and Chou, 1991; Chiu et al., 1996]. Geochemical analysis has shown that total organic carbon (TOC) in all stratigraphic sequences is generally less than 1.0% (Table 1). Rock Eval pyrolysis and computational analysis have shown that the kerogen in the Taiwan oil field is of continental origin and has a high oxygen content. The activation energy of the dominant fraction centers around 62 kcal/mol in most rocks, suggesting that significant maturation is necessary to generate the expected amount of oil. The Arrhenius constant is between 2.6×10^{15} and 2.1×10^{16} s^{-1} [Chiu et al., 1996]. In our submodel, the kinetic parameter values of the Talu Shale [Chiu et al., 1996] are used as representative values because the kinetic parameter values of several formations are unknown. The same temperature history used for the smectite dehydration model (Fig. 2) was also used for the kinetic hydrocarbon generation reaction.

5-4. Viscosity and thermal effect

The viscosity of water μ depends on temperature T, as follows [Fontaine et al., 2001]:

$$\mu = 2.414 \times 10^{-5} \times 10^{(247.8)/(T+133)}. \qquad (16)$$

The pressure dependence of viscosity is not considered, because the pressure sensitivity of viscosity is small compared with its temperature dependence. The geothermal gradient in our study area in the Western Foothills is from 25 to 38 °C/km [Suppe and Wittke, 1977], and fluid viscosity decreases by 1 order of magnitude between the surface and 8 km depth, from 0.001 to 0.0001 Pa·s.

6. Numerical simulation result

6-1. Overpressure history and distribution

The numerical simulation results for overpressure estimation in the north-central Western Foothills, in the case of no fluid flux at the bottom of the sedimentary basin sequence, are shown in Figure 8a. No overpressure was generated from 30 to 3 Ma at any depth, and then overpressure was rapidly generated from 3 Ma (Fig. 8a). The period of rapid overpressure generation coincides with the period of rapid sediment accumulation due to the early Late Miocene collision, which caused a large amount of orogenic sediment to be deposited in the Western Foothills region. After the sedimentation rate reaches 0 m/My, excess fluid pressure dramatically drops in all formations, and a large amount of the overpressure is dissipated. The predicted fluid pressure distributions at present (0 Ma) and at 0.8 Ma are plotted in Figure 8b. Notice that the observed overpressure data shown in Figure 8b [Suppe and Wittke, 1977] are shifted to match the stratigraphic horizons with our numerical simulation curves (the observed data were shifted downward because erosion occurred at some observation sites and the erosion rate varied among locations). The numerically modeled curves in Figure 8b show lower values at depth than the observed overpressure values. The values indicated by the fluid pressure curve at the maximum fluid pressure during the sedimentation period (0.8 Ma) are also smaller than the observed values (Fig. 8b), though the trend of these curves at 0.8 Ma is similar to the observed trend.

Figure 9 illustrates the numerically modeled overpressure distribution at 0.8 Ma. We calculated the overpressure for several values of α_f, n, and Φ_k (see Table 2) to investigate the influence of sediment compaction, geothermal pressuring, clay mineral dehydration, and hydrocarbon generation on overpressure generation in this oil field. In each case, overpressure was generated below 4 to 5 km depth, and the overpressure increased with depth. The transition zone in the numerical simulation results is around the Talu Shale and Peiliao formations, which is consistent with the observed data. The difference between curve A, which includes only sediment loading as a generation factor, and curve B, which also includes the geothermal expansion of fluid, is small, suggesting that the thermal expansion of water did not significantly contribute to overpressure generation. Curves C and D include the clay mineral dehydration factor, and much more overpressure is generated compared with curves A and B.

Curves E and F add the hydrocarbon generation factor to curve B. These results indicate that clay mineral dehydration controls excess fluid pressure more than hydrocarbon generation. However, in each case, the generated overpressure is significantly smaller than the observed overpressure and it decreases rapidly by 0 Ma.

Figure 10 show simulated results when continuous fluid influx at the bottom of the sedimentary basin is incorporated; we assumed the fluid influx to be constant throughout the sedimentation history (30 to 0 Ma). The evolutionary history of the simulated overpressure when a fluid influx of 1×10^{-12} m/s is assumed is shown in Figure 10a. Overpressure is dramatically generated from 3 Ma, just as when no flux is assumed, but the amount of overpressure generated is much larger than that generated when no flux is assumed. Overpressure begins to decrease from 0.8 Ma, but remains at a high level until the present. The stratigraphic distribution of the overpressure is shown in Figure 10b. With an increase in the fluid influx, the predicted overpressure also increases and produces a fluid pressure trend similar to the observed trend.

6-2. Smectite–illite transition

The estimated volume fraction transition of smectite in this area at various stratigraphic ages is shown in Figure 11. The initial volume fraction of smectite was assumed to be constant at 0.2 in all formations [Wangen, 2001]. Most of the smectite is dehydrated at the depth of around 3 to 4 km at all ages. After the cessation of sedimentation in 0.8 Ma, the transition depth became shallower; the current transition depth is at around 3.5 km. The numerical simulation results show that at present most smectite has disappeared at 5 km depth. The results of a qualitative analysis of the clay mineral composition of all formations by X-ray diffraction indicate that smectite has disappeared from the Kuanyinshan Sandstone and below, which is consistent with the numerical simulation curve, though illite is present at all depths.

7. Discussion

The overpressure in the Western Foothills predicted by numerical modeling that incorporates experimental data is much lower than the overpressure observed in boreholes if no fluid influx at depth is assumed. On the other hand, when a fluid influx is assumed, the model results show that a large amount of fluid pressure is produced and maintained for a long time, a result that is consistent with the observed overpressure data. Therefore, a continuous fluid influx may be the main factor accounting for the maintenance of overpressure in the Taiwan oil field. There are several lines of geological evidence that a large amount of water can be discharged from the deep crust [Rumble, 1994]. Prograde metamorphism due to subduction of the crust likely results in the release of water by a dehydration reaction [Ague et al. 1998]. In the case of the Western Foothills, part of the continental Eurasian plate subducts along with the Philippine Sea plate [Lallemand et al., 2001]. Therefore, muscovite and biotite of continental origin may be the source minerals for metamorphic dehydration [Wong et al., 1997]. Some of the marine sediments of the subducting Philippine Sea plate may also have released water in response to regional metamorphism. The décollement and the plate boundary may be the pathway for influx of deeply sourced fluid. We also propose that additional fluids may migrate vertically through the lower sedimentary sequence or through the normal faults that formed along with the South China Sea in the middle Tertiary [Mouthereau and Lacombe, 2006].

The predicted fluid pressure increase is hydrostatic at shallow depths, and overpressure is gradually generated at the depths of the Middle Miocene formations, similar to the observed pressure trend. Furthermore, we could not identify any clear impermeable sealing layer. These results indicate the importance of stratigraphic change in transport properties, which in general decrease with depth as a result of time- and depth-dependent consolidation, as pointed out by Bethke and Corbet [1988]. If the transport properties were constant at all depths, overpressure would be generated at a shallower depth and would become constant at depth [Bredehoeft and Hanshaw, 1968]. All transport properties showed stratigraphic decreases, though the amount of decrease differed among parameters. Both permeability and specific storage are diffusive parameters that affect hydraulic conductivity (= $k/Ss \cdot \mu$), but the change in permeability was much larger than that in specific storage. This suggests that permeability contributes more to the shape of the pressure distribution than specific storage. Permeability showed a decrease of about 6 to 7 orders of magnitude over a depth range of 8 km. This depth dependence is not much different from the decrease of about 3 orders of magnitude over a depth range of 4 km in the Denver basin reported previously [Beltz and Bredehoeft, 1988], though the permeability reduction with depth is larger in some other basins [Dutton and Diggs, 1992; Bour and Lerche, 1994]. The nonlinearity of the loading efficiency indicates that it becomes more difficult to generate overpressure by sediment loading with increasing depth.

Our numerical simulation shows that a large amount of overpressure was generated by 0.8 Ma as a result of the acceleration of sediment loading from 3 Ma. The burial rate of 1500 m/My during the Late Pliocene is relatively high compared with that in many other basins [McPherson and Garven, 1999; McPherson and Bredehoeft, 2000], but it is comparable to the rate in the Gulf Coast Basin, where anomalous high pressure has also evolved (>1000 m/My) [Bethke, 1986; Harrison and Summa, 1991]. This result also suggests that rapid sedimentation and the corresponding increase in sediment thickness was required to maintain the excess fluid pressure at depth in the Western Foothills.

7-1. Potential errors in the hydraulic parameters

Our numerical analysis results showed that an influx of extra fluid can explain the maintenance of overpressure in the Western Foothills, but the hydraulic parameter values evaluated in the laboratory tests may incorporate certain errors. Correction of these errors might allow the overpressure distribution to be explained without the assumption of a fluid influx. Estimation of in situ transport properties by ex situ laboratory tests may have introduced errors into the data. In general, permeability evaluated by in situ measurements is higher than that determined by laboratory measurement because of enhanced flow in mesoscopic- and macroscopic-scale fractures in laboratory samples [Brace, 1980]. Moreover, the surface-quarried samples used for the laboratory tests experienced unloading and weathering, which might have produced micro- and macrocracks, causing lower pressure sensitivity of permeability and higher permeability values [Morrow and Lockner, 1994]. The stratigraphic variations in the permeability and porosity data (Fig. 6) are scattered, which can be explained by the non-uniformity of the rock samples. It is also probable that the larger values were caused by microcrack enhancements of the surface-quarried samples. In addition, the harmonic mean of the individual permeability values is a more suitable metric for describing flow across bedding layers, and results in a lower value than the arithmetic mean. Therefore, the lower values we chose for the numerical analysis are likely reasonable parameter values to use for describing realistic conditions at depth.

Intact core samples might yield more realistic measurement values, and the differences in the hydraulic properties between surface and core samples should be determined in a future study. We estimated permeability from a gas flow experiment, and converted the obtained gas permeability values to water permeability using the Klinkenberg equation (equation 2). In general, in our specimens, the Klinkenberg effect caused a difference of less than 1 order of magnitude between gas and water permeability, but Faulkner and Rutter [2000] suggest that water permeability is typically 1 or more order of magnitude less than gas permeability because of the reduction of effective pore diameter caused by the adhesion of water molecules to the crystal surface, rather than because of the Klinkenberg effect. These probable errors may have caused overestimation of the permeability values used in the basin model. However the numerical results in which permeability was underestimated (curves E and F in Fig. 10a) do not agree with the observed data, indicating that any permeability errors introduced by the use of laboratory test results of surface-derived samples were not critical in the excess pressure estimation.

Another possible source of error is our application of isotropic parameters measured by isotropic compaction tests to the numerical solutions. Ideally, uniaxial permeability and drained compressibility parameters should be used in a one-dimensional compaction flow model [Gibson, 1958], which assumes that sedimentation is constrained laterally. However, in the case of the Western Foothills, lateral compression by tectonic loading is effective, and the appropriate hydraulic parameter values might lie between the isotropic and uniaxial values. Though differences in permeability between isotropic and uniaxial conditions are poorly documented, the differences in poroelastic parameter values between isotropic and uniaxial conditions have been theoretically investigated [Wang, 2000]. For example, loading efficiency (Skempton's coefficient, B) under uniaxial strain is smaller than that under isotropic conditions. Similarly, isotropic specific storage values (*Ss*; our study) are larger than uniaxial specific storage values. These findings suggest that the use of uniaxial parameters would result in less overpressure generation being predicted. Therefore, the influence of anisotropic stress on hydraulic properties was not critical in the model.

7-2. Other possible sources of error

We simplified the hydrocarbon generation model, though the simplification is not critical because of the low TOC of the formations [Luo and Vasseur, 1996]. Development of impermeable thrust fault layers is another potential mechanism of overpressure maintenance. However, no large thrust fault has been found near the overpressure transition horizons in the study area [Fig. 2, Namson, 1982]. Another limitation is that we assumed only vertical one-dimensional flow. Two- or three-dimensional models with lateral flow are required for a more realistic analysis. Moreover, several of the well sites have been tectonically uplifted and eroded, causing dissipation of overpressure [Neuzil and Pollock, 1983]. Therefore, erosion might have caused a drastic reduction of overpressure. Nevertheless, large excess pore pressure is maintained at present, which implies the importance of a fluid influx at depth.

We assumed that the sedimentation rate became 0 at about 0.8 Ma, perhaps in association with the switch from sedimentation to folding and thrusting. If the initiation of folding and thrusting was sufficiently widespread in this area, sedimentation would have stopped and the locus of deposition would have moved westward or southward. However, during natural tectonic processes, temporal and spatial variations in deposition and exhumation rates are complicated.

The change in the deformation pattern at about 0.8 Ma might have been associated with a transition from a vertically orientated σ_1 (sediment accumulation phase) to a horizontally oriented σ_1 (thrusting phase), which might have affected the pore pressure distribution. Tectonic deformation may lead to further compaction of sedimentary rock, decreasing its permeability [Zhu and Wong, 1997]. However, if the rock is loaded beyond the critical stress, a significant permeability increase by dilation or microcrack enhancement is predicted to occur. In either case, permeability and porosity changes by tectonic deformation should be considered in future basin analyses.

8. Conclusion

We evaluated the detailed vertical stratigraphic variation of hydraulic properties in the oil fields of north-central Taiwan to estimate the overpressure generation process. All hydraulic transport properties showed strong stratigraphic dependence. Permeability decreased sharply with an increase in burial depth, and the permeability of the basement formation became 7 orders of magnitude smaller than that of the youngest sediments in the Western Foothills. Specific storage and Skempton's coefficient also showed stratigraphic dependence, though they exhibited a smaller sensitivity than permeability. Our experimental data also suggested that specific storage and Skempton's coefficient when estimated by using Athy's law, which is empirically derived, were overestimated compared with laboratory data. A one-dimensional compaction flow analysis incorporating the laboratory-evaluated parameter values showed that continuous fluid influx at depth may be an important cause of the observed overpressure maintenance under the current stable or erosional conditions, and vertical changes in permeability may also restrict the vertical fluid pressure distribution trend. Predicted overpressure generation increases dramatically from 3 Ma, when sediment accumulation was accelerated by the severe tectonic collision between the Luzon arc and the Asian continent. A more advanced two- or three-dimensional analysis considering multiple flow systems is necessary to confirm the mechanism of overpressure generation in the north-central Western Foothills.

Acknowledgments

This work was supported by the Interchange Association, Japan (IAJ), along with the Japanese-Taiwanese exchange program. The Chinese Petroleum Corporation gave us tremendous support and many scientific suggestions for our field research. Professor Wei-Min Chen of the National Central University of Taiwan and his students also gave us support during

Tanikawa's visit to Taiwan. We extend our appreciation to all of the members of our laboratory at Kyoto University for many scientific discussions.

Appendix A: Pressure generation equation (11)

The numerical expression of pressure generation in a thick sedimentary basin (equation 11) is a simplification of Wangen's model [2001] that includes the overpressure generation factors of sediment loading, thermal expansion, clay dehydration, and hydrocarbon generation. The conservation law of fluid phase for porous media is described as follows:

$$\frac{\partial}{\partial t}\left(\Phi\rho_f\right)+\frac{\partial}{\partial z}\left(\Phi\rho_f V_f\right)=q_f\,, \qquad \text{(A1)}$$

where Φ is the bulk volume fraction of the pore fluid or porosity, ρ_f is the density of the fluid, V_f is the velocity of the fluid, and q_f is the specific discharge of the fluid, which gives the rate of production or consumption of the fluid in units of mass per bulk volume and time. The conservation law of the solid phase (matrix) is similarly described:

$$\frac{\partial}{\partial t}\left(\Phi_s\rho_s\right)+\frac{\partial}{\partial z}\left(\Phi_s\rho_s V_s\right)=q_s\,, \qquad \text{(A2)}$$

where Φ_s is the bulk volume fraction of the grain matrix, ρ_s is the density of the matrix, V_s is the velocity of the matrix, and q_s is the specific discharge of the matrix. q_s is the rate at which the minerals are formed or decomposed in units of mass per bulk volume and time. The relationship between porosity and the matrix volume fraction is,

$$\Phi + \Phi_s = 1. \tag{A3}$$

Equation (A1) can be transformed to,

$$\frac{\partial}{\partial t}\left(\Phi \rho_f\right) + \frac{\partial}{\partial z}\left[\rho_f \left(\Phi V_f - \Phi V_s\right)\right] + \frac{\partial}{\partial z}\left(\rho_f \Phi V_s\right) = q_f. \tag{A4}$$

When both the operator Δ/dt of the material derivative,

$$\frac{\Delta}{dt} = \frac{\partial}{\partial t} + V_s \frac{\partial}{\partial z} \quad , \tag{A5}$$

and equation (A3) are applied, equations (A4) and (A2) respectively become,

$$\frac{\Phi}{\rho_f}\frac{\Delta \rho_f}{dt} + \frac{\Delta \Phi}{dt} + \frac{1}{\rho_f}\frac{\partial}{\partial z}\left[\rho_f \Phi \left(V_f - V_s\right)\right] + \Phi \frac{\partial V_s}{\partial z} = \frac{q_f}{\rho_f} \tag{A6}$$

$$-\frac{\Delta \Phi}{dt} + \frac{(1-\Phi)}{\rho_s}\frac{\Delta \rho_s}{dt} + (1-\Phi)\frac{\partial V_s}{\partial z} = \frac{q_s}{\rho_s}. \tag{A7}$$

The combination of equations (A6) and (A7) gives the following equation:

$$\frac{\Phi}{\rho_f}\frac{\Delta \rho_f}{dt} + \frac{1}{1-\Phi}\frac{\Delta \Phi}{dt} - \frac{\Phi}{\rho_s}\frac{\Delta \rho_s}{dt} + \frac{1}{\rho_f}\frac{\partial}{\partial z}\left[\rho_f \Phi \left(V_f - V_s\right)\right] = \frac{q_f}{\rho_f} - \frac{\Phi}{1-\Phi}\frac{q_s}{\rho_s}. \tag{A8}$$

Darcy's law, which is related to fluid and solid velocities, can be written as,

$$\Phi\left(V_f - V_s\right) = -\frac{k}{\mu}\frac{\partial}{\partial z}P, \tag{A9}$$

where k is (intrinsic) permeability, μ is the fluid viscosity, and P is the pore pressure. Equation (A9) assumes only one-dimensional flow in a vertical direction.

Drained pore compressibility, β_Φ, can be described as follows:

$$\beta_\Phi = -\frac{1}{1-\Phi}\frac{\partial \Phi}{\partial Pe}, \tag{A10}$$

where Pe is the effective pressure, which is described in terms of pore pressure, P, and confining pressure, Pc, as

$$Pe = Pc - P. \tag{A11}$$

Fluid compressibility, β_f, and the thermal expansion coefficient of water, α_f, can be respectively expressed as

$$\beta_f = -\frac{1}{\rho_f}\frac{\partial \rho_f}{\partial P} \tag{A12}$$

$$\alpha_f = \frac{1}{\rho_f}\frac{\partial \rho_f}{\partial T}. \tag{A13}$$

By combining equations (A12) and (A13), the following equation is obtained:

$$\frac{1}{\rho_f}\frac{\partial \rho_f}{\partial t} = \beta_f \frac{\partial P}{\partial t} - \alpha_f \frac{\partial T}{\partial t}. \tag{A14}$$

When the porosity change is related to the mechanisms of mechanical compaction, clay mineral dehydration, and oil generation, the time dependency of the porosity change can be described as follows:

$$\frac{\Delta\Phi}{dt}=\frac{\Delta\Phi_{mech}}{dt}+\frac{\Delta\Phi_{deh}}{dt}+\frac{\Delta\Phi_{oil}}{dt}=-\beta_{\Phi}\left(1-\Phi\right)\left(\frac{\Delta Pc}{dt}-\frac{\Delta P}{dt}\right)+\frac{\Delta\Phi_{deh}}{dt}+\frac{\Delta\Phi_{oil}}{dt}. \quad \text{(A15)}$$

The source term of the matrix can be also described as

$$\frac{q_s}{\rho_s}=\frac{q_{deh}}{\rho_{deh}}+\frac{q_{oil}}{\rho_{oil}}. \quad \text{(A16)}$$

Substituting equations (A9) to (A16) into (A8), we obtain

$$\left(\Phi\beta_f+\beta_{\Phi}\right)\frac{\Delta P}{dt}=\frac{\partial}{\partial z}\left(\frac{k}{\mu}\frac{\partial}{\partial z}P\right)+\Phi\alpha_f\frac{\Delta T}{dt}+\beta_{\Phi}\frac{\Delta Pc}{dt}-\frac{1}{1-\varphi}\left(\frac{\Delta\Phi_f}{dt}+\frac{\Delta\Phi_{oil}}{dt}\right)+\frac{q_f}{\rho_f}-\frac{\Phi}{1-\Phi}\left(\frac{q_{deh}}{\rho_{deh}}+\frac{q_{oil}}{\rho_{oil}}\right)$$

(A17).

In equation (A17), we assumed that the change in matrix density due to compression and other mechanisms is sufficiently small to be considered zero. If the poroelastic parameters specific storage, *Ss*, and Skempton's coefficient, *B*, are used, equation (A17) becomes:

$$Ss\frac{\Delta P}{dt}=\frac{\partial}{\partial z}\left(\frac{k}{\mu}\frac{\partial}{\partial z}P\right)+\Phi\alpha_f\frac{\Delta T}{dt}+BSs\frac{\Delta Pc}{dt}+Q_{deh}+Q_{oil}, \quad \text{(A18)}$$

where the pore pressure generation terms for clay mineral dehydration, Q_{deh}, and hydrocarbon generation, Q_{oil}, can be respectively given as

$$Q_{deh}=\frac{q_f}{\rho_f}-\frac{1}{1-\Phi}\frac{\Delta\Phi_{deh}}{dt}-\frac{\Phi}{1-\Phi}\frac{q_{deh}}{\rho_{deh}} \quad \text{(A19)}$$

$$Q_{oil}=\frac{q_s}{\rho_s}-\frac{1}{1-\Phi}\frac{\Delta\Phi_{oil}}{dt}-\frac{\Phi}{1-\Phi}\frac{q_{oil}}{\rho_{oil}}. \quad \text{(A20)}$$

Appendix B: Pore pressure generation terms for clay mineral dehydration and hydrocarbon generation

The clay mineral dehydration reaction in our basin model is based on the assumption that smectite can be transformed to illite and water by a kinetic reaction. For the dehydration reaction, we simply assumed that 1 mol of smectite can be changed to 1 mol of illite and *n* mol of water. The source term for the smectite, q_{sm}/ρ_{sm}, which is the rate of volume loss of smectite per bulk volume of rock is described as

$$\frac{q_{sm}}{\rho_{sm}} = \frac{q_{deh}}{\rho_{deh}} = \frac{\Delta\Phi_{sm}}{dt}. \tag{B1}$$

The source term for the illite is described as

$$\frac{q_{il}}{\rho_{il}} = -\frac{V_{il}}{V_{sm}} \frac{q_{sm}}{\rho_{sm}}, \tag{B2}$$

where V_{il}/V_{sm} is the molar volume ratio of illite to smectite. The specific discharge of fluid due to dehydration is described as follows:

$$\frac{q_f}{\rho_f} = -n \frac{V_f}{V_{sm}} \frac{s_{sm}}{\rho_{sm}}, \tag{B3}$$

where V_f/V_{sm} is the molar volume ratio of water to smectite. The change in porosity by the dehydration reaction, $\Delta\Phi_{deh}/dt$, can be caused by the change in solid volume, assuming the conservation of bulk volume. Therefore, this porosity change can be described as

$$\frac{\Delta\Phi_{deh}}{dt} = \frac{\Delta\Phi_{sm}}{dt} - \frac{\Delta\Phi_{il}}{dt} = \left(1 - \frac{V_{il}}{V_{sm}}\right) \frac{q_{sm}}{\rho_{sm}}. \tag{B4}$$

From equations (B1) to (B4), Q_{deh} in equation (A19) is expressed as follows:

$$Q_{deh} = \frac{q_{sm}}{\rho_{sm}}\left(-n\frac{V_f}{V_{sm}} - \frac{V_{il}}{V_{sm}} + 1\right). \tag{B5}$$

If no volume change between illite and smectite is assumed, that is, $V_{il} = V_{sm}$, then equation (14) is formed by using equation (B5).

Equation (15) is formed in the same way as equation (14) when the relationship

$$\frac{V_{oil}}{V_{kr}} = \frac{\rho_{kr}}{\rho_{oil}} \tag{B6}$$

is used.

References

Ague, J. J., J. Park, and D. M. Rye (1998), Regional metamorphic dehydration and seismic hazard, *Geophys. Res. Lett., 25,* 4221–4224.

Athy, L. F. (1930), Density, porosity, and compaction of sedimentary rocks, *AAPG Bull., 14,* 1–22.

Audet, D. M. (1995), Mathematical modeling of gravitational compaction and clay dehydration in thick sediment layers, *Geophys. J. Int., 122,* 283–298.

Belitz, K., and J. D. Bredehoeft (1988), Hydrodynamics of the Denver basin: an explanation of subnormal fluid pressures, *AAPG Bull., 72,* 1334–1359.

Bethke, C. M. (1986), Inverse hydrologic analysis of the distribution and origin of gulf coast-type geopressured zones, *J. Geophys. Res., 91,* 6535–6545.

Bethke, C. M., and F. Corbet (1988), Linear and nonlinear solutions for one-dimensional compaction flow in sedimentary basins, *Water Resources Res., 24,* 461–467.

Birch, F. (1966), Compressibility, Elastic constants, in *Handbook of Physical Constants*, edited by S. P. Clark, pp. 97-173, Geological Society of America Memoir 97.

Bour, O., and I. Lerche, (1994), Numerical modelling of abnormal fluid pressures in the Navarin Basin, Bering Sea, *Marine and Petroleum Geology, 11,* 491-500.

Brace, W. F. (1980) Permeability of Crystalline and Argillaceous Rocks, *Int. J. Rock Mech. Min. Sci. and Geomech. Abst. 17*, 241-251.

Bredehoeft, J. D., and B. B. Hanshaw (1968), On the maintenance of anomalous fluid pressures: I. Thick sedimentary sequences: *Geol. Soc.*

Am. Bull., 79(9), 1097–1106.

Bredehoeft, J. D., J. B. Wesley, and T. D. Fouch (1994), Simulations of the origin of fluid pressure, fracture generation, and the movement of fluids in the Uinta basin, Utah, *AAPG Bull., 78*, 1729–1747.

Chiu, J. H., and T. H. Chou (1991), Geochemical modeling for the petroleum generation potential of lower Miocene formations in Tiehchenshan Field, *Petroleum Geology of Taiwan, 26,* 93–108.

Chiu, J. H., C. L. Kuo, and T. H. Chou (1996), The kinetic modeling of hydrocarbon generation in source rock of Taiwan area, *Petroleum Geology of Taiwan, 30,* 51–78.

Dadson, S. J., N. Hovius, H. Chen, W. B. Dade, M.-L. Hsieh, S. D. Willett, J.-C., Hu, M.-J., Horng, M.-C., Chen, C.P., Stark, D., Lague, and J.-C., Lin (2003), Links between erosion, runoff variability and seismicity in the Taiwan orogen, *Nature*, *426*, 648–651.

David, C., T. F. Wong, W. Zhu., and J. Zhang (1994), Laboratory measurement of compaction-induced permeability change in porous rocks: implications for the generation and maintenance of pore pressure excess in the crust, *Pure Appl. Geophys., 143,* 425–456.

Davis, D., J. Suppe, and F. A. Dahlen (1983), Mechanics of fold-and-thrust belts and accretionary wedges, *J. Geophys. Res., 88,* 1153–1172.

Dutton, S. P., and T. N. Diggs (1992), Evolution of porosity and permeability in the lower cretaceous Travis Peak Formation, East Texas, *AAPG Bull., 76*, 252–269.

Elliott, W. C., J. L. Aronson, G. Matisoff, and D. L. Gautier (1991), Kinetics of the smectite to illite transition in the Denver Basin: Clay mineral, K-Ar data, and mathematical model results, *AAPG Bull., 75,* 436–462.

Faulkner, D. R., and E. H. Rutter (2000), Comparisons of water and argon permeability in natural clay-bearing fault gouge under high pressure at 20 degrees C, *J. Geophys. Res., 105,* 16415–16426.

Fontaine, F. J., M. Rabinowicz, and J. Boulègue (2001), Permeability changes due to mineral diagenesis in fractured crust; implications for hydrothermal circulation at mid-ocean ridges, *Earth Planet. Sci. Lett., 184*(2), 407–425.

Freed, R. L., and D. R. Peacor (1989), Geopressured shale and sealing effect of smectite to illite transition, *AAPG Bull.*, *73*, 1223– 1232.

Furbish, D. J. (1997), Fluid physics in geology; an introduction to fluid motions on earth's surface and within its crust, 476 pp., Oxford University Press, New York.

Gibson, R. E. (1958), The progress of consolidation in a clay layer increasing in thickness with time, *Géotechnique, 8,* 171–182.

Green, D. H., and H. F. Wang (1986), Fluid pressure response to undrained compression in saturated sedimentary rock, *Geophysics, 51*(4), 948–956.

Harrison, W. J., and L. L. Summa (1991), Paleohydrology of the Gulf of Mexico Basin, *Am. J. Sci.*, *291,* 109–176.

Hart, B. S., P. B. Flemings, and A. Deshpande (1995), Porosity and pressure: role of compaction disequilibrium in the development of geopressures in a Gulf Coast Pleistocene basin, *Geology, 23*, 45–48.

Hunt, J. M. (1990), Generation and migration of petroleum from abnormally pressured fluid compartments, *AAPG Bull.*, *74,* 1–12.

Ingebritsen, S. E., and C. E. Manning (1999), Geological implication of a permeability-depth curve for the continental crust, *Geology, 27,* 1107–1110.

Klinkenberg, L. J. (1941), The permeability of porous media to liquids and gases, American Petroleum Institute, Drilling and Productions Practices, 200–213.

Lallemand, S., C.-S. Liu, and Y.-B. Tsai. (2001), Active subduction and collision in Southeast Asia, *Tectonophysics*, 333, 1–7.

Law, B. E., and C. W. Spencer (1998), Abnormal pressures in hydrocarbon environments, *in* Law, B. E., G. F. Ulmishek, and V. I. Slavin eds., Abnormal pressures in hydrocarbon environments, *AAPG Memoir, 70*, 1–11.

Lee, J. F. (2000), Geologic map of Taiwan, Tungshih Sheet, Taipei, Central Geological Survey of Taiwan, 25, 1:50,000.

Luo, X., and G. Vasseur (1992), Contribution of compaction and aquathermal pressuring to geopressure and the influence of environmental conditions, *AAPG Bull, 76,* 1550–1559.

Luo, X., and G. Vasseur (1996), Geopressuring mechanism of organic matter cracking: Numerical modeling, *AAPG Bull, 80,* 856–874.

McPherson, B. J. O. L., and J. D. Bredehoeft (2001), Overpressures in the Uinta basin, Utah; Analysis using a three-dimensional basin evolution model, *Water Resources Res., 37,* 857–871.

McPherson, B. J. O. L., and J. D. Garven (1999), Hydrodynamics and overpressure mechanisms in the Sacramento basin, California. *Am. J. Sci., 299*, 429–66

Moore, J. C., and D. M. Saffer (2001), Updip limit of the seismogenic zone beneath the accretionary prism of southwest Japan: An effect of diagenetic to low-grade metamorphic processes and increasing effective stress, *Geology, 29,* 183–186.

Morrow, C. A., and D. A. Lockner (1994), Permeability differences between surface-derived and deep drillhole core samples, *Geophys. Res. Lett., 21*, 2151–2154.

Mouthereau, F., and O. Lacombe (2006), Inversion of the Paleogene Chinese continental margin and thick-skinned deformation in the Western Foreland of Taiwan, Journal of Structural Geology, *28*, 1977–1993.

Namson, J. S. (1982), Studies of the structure, stratigraphic record of plate interaction and role of pore-fluid pressure in the active fold and thrust belt of Taiwan and a study of manganese deposits from northern

California, Ph. D. thesis, 302 pp., Princeton University, Princeton, New Jersey.

Neuzil, C. E., and D. W. Pollock (1983), Erosional unloading and fluid pressures in hydraulically “tight” rocks, *J. Geology, 91,* 179–193.

Osborn, M. J., and R. E. Swarbrick (1997), Mechanisms for generating overpressure in sedimentary basins: a reevaluation: *AAPG Bull, 81*(6), 1023–1041.

Oung, J. N. (2000), Two-dimensional basin modeling—a regional study on hydrocarbon generation, offshore Taiwan, *Petroleum Geology of Taiwan, 34,* 33–54.

Pytte, A. M., and R. C. Reynolds (1988), The thermal transformation of smectite to illite, in *Thermal Histories of Sedimentary Basins*, edited by N. D. Naeser and T. H. McCulloh, pp. 133-140, Springer-Verlag, New York.

Rumble, D., III (1994), Water circulation in metamorphism. *J. Geophys. Res., 99,* 15499-15502.

Scheidegger, A. E. (1974), *The Physics of Flow through Porous Media*, 3rd Edition, 102 pp, University of Toronto Press, Toronto.

Suppe, J., and J. H. Wittke (1977), Abnormal pore-fluid pressures in relation to stratigraphy and structure in the active fold-and-thrust belt of northwestern Taiwan, *Petroleum Geology of Taiwan, 14,* 11–24.

Teng, L. S. (1990), Geotectonic evolution of late Cenozoic arc-continent collision in Taiwan, *Tectonophysics, 183,* 57–76.

Terzaghi, K. (1925), Principles of soil mechanics: IV. Friction in sand and clay, *Eng. News Record, 95,* 1026–1029.

Wang, H. F. (2000), *Theory of Linear Poroelasticity: With Applications to Geomechanics and Hydrogeology*, Princeton Series in Geophysics, 287 pp, Princeton University Press, Princeton.

Wangen, M. (2001), A quantitative comparison of some mechanisms generating overpressure in sedimentary basins, *Tectonophysics, 334,* 211–234.

Wibberley, C. (2002), Hydraulic diffusivity of fault gouge zones and implications for thermal pressurization during seismic slip, *Earth Planets Space, 54,* 1153–1171.

Wong, T. F., S.-C. Ko, and D. L. Olgaard (1997), Generation and maintenance of pore pressure excess in a dehydrating system2.

Theoretical analysis, *J. Geophys. Res.*, *102*, 841–852.

Yu, S. B., L. C. Kuo, R. S. Punongbayan, and E. G. Ramos (1999), GPS observation of crustal deformation in the Taiwan-Luzon region, *Geophys. Res. Lett., 26,* 923–926.

Zhu, W., and T. F. Wong (1997), The transition from brittle faulting to cataclastic flow: Permeability evolution, *J. Geophys. Res.*, *102*, 3027–3041.

Captions

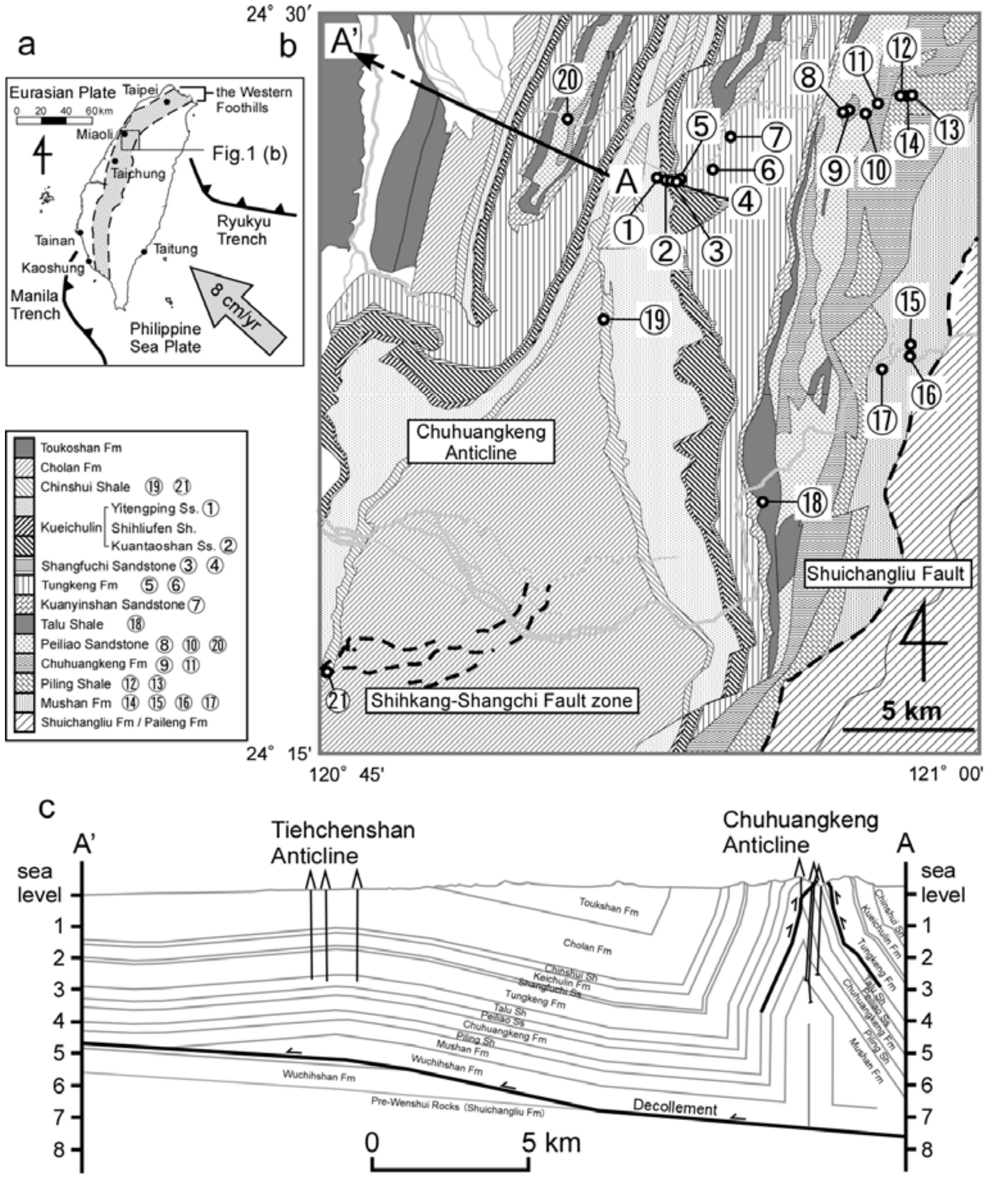

Figure 1. (a) Geotectonic setting of Taiwan. (b) Geological map of the Tungshih study area [Lee, 2000] in the north-central Western Foothills. The sampling locations of the sedimentary rocks used for the laboratory experiments are plotted (circled numbers). (c) Vertical cross-section of representative oil well sites in the north-central Western Foothills (modified from Namson, 1982). Typically, borehole sites are on anticlines.

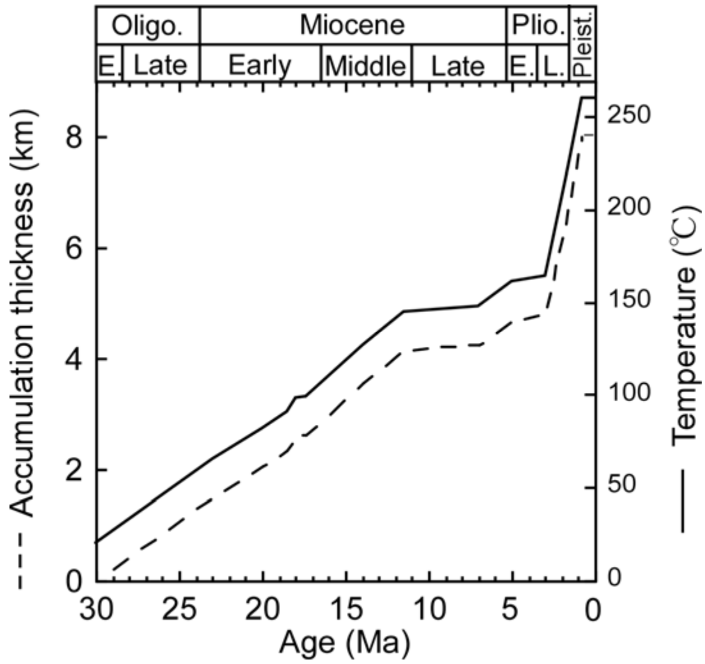

Figure 2. Sediment accumulation history and temperature history at the bottom of the sedimentary sequence in the Western Foothills, compiled from Lee [2000]. A geothermal gradient of 30 °C/km is assumed.

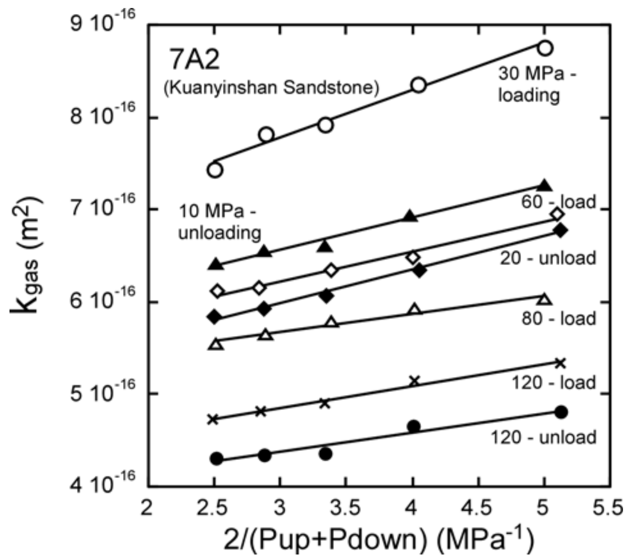

Figure 3. Inverse of average pore pressure plotted against permeability to nitrogen gas for one pressure cycling test of sample 7A2 (see Figure 1b for the sample location of the circled number 7). The straight fitted lines suggest that the experimental results are consistent with the Klinkenberg equation (2). Permeability to water can be estimated from the slopes.

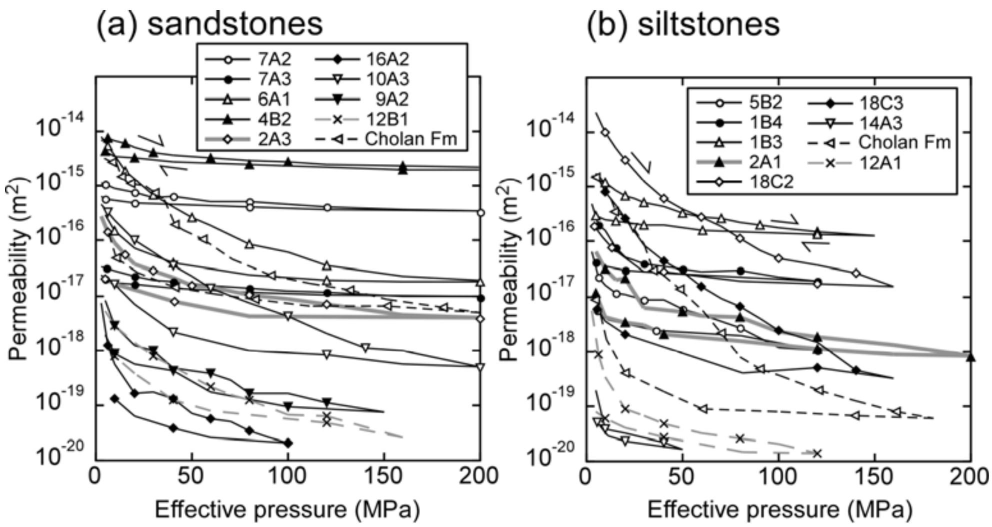

Figure 4. Permeability as a function of effective pressure during one pressure cycling test for (a) sandstones and (b) siltstones.

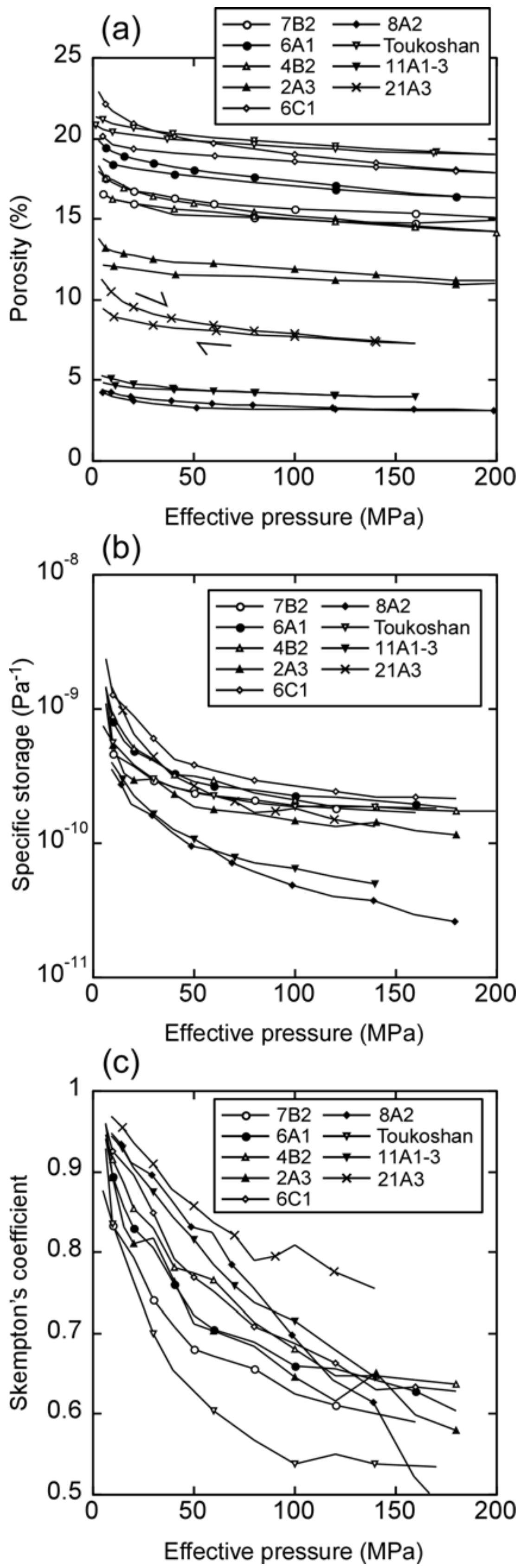

Figure 5. (a) Porosity, (b) specific storage, and (c) Skempton's coefficient as

a function of effective pressure in sandstones. Specific storage was evaluated by using equation (4) and Skempton's coefficient by using equation (6). Drained pore compressibility was estimated from porosity.

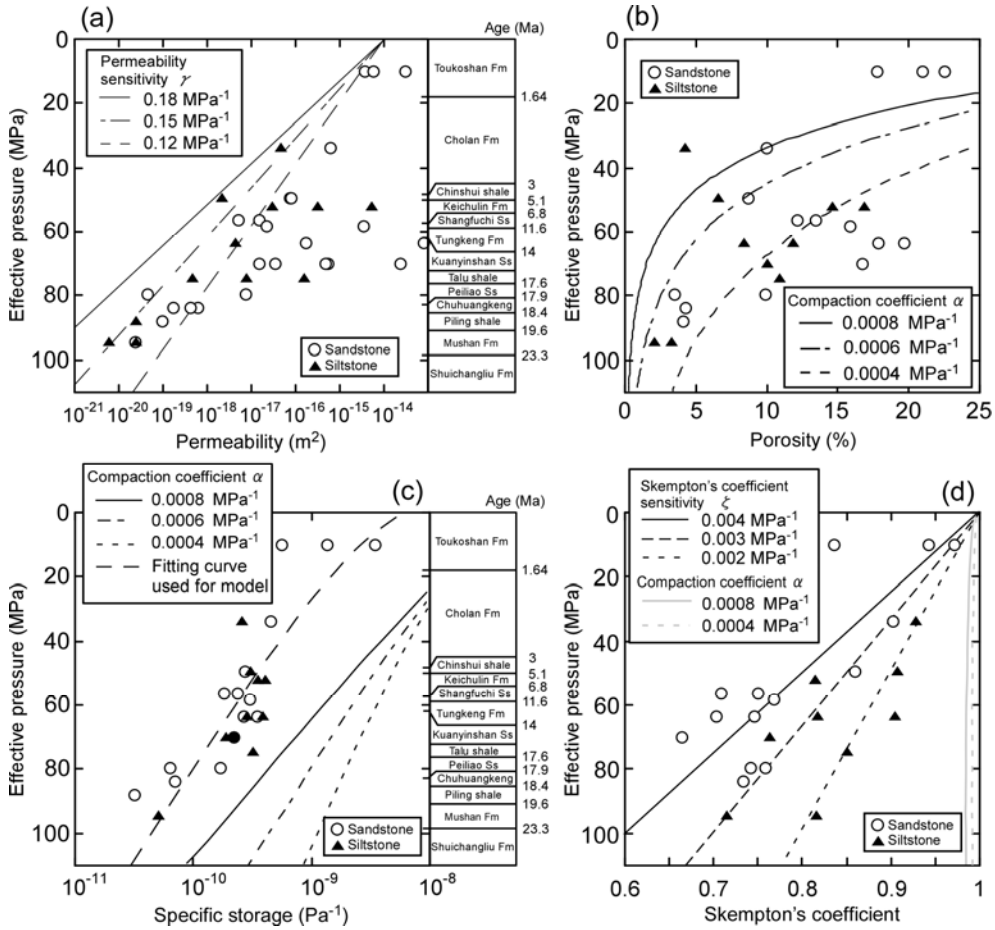

Figure 6. Stratigraphic variation in (a) permeability, (b) porosity, (c) specific storage, and (d) Skempton's coefficient in rocks of the Western Foothills, described as a function of effective pressure. Each data point is plotted at the point where the effective pressure is equivalent to maximum burial depth,

assuming hydrostatic conditions. Approximation curves of equations (7) to (10) for various values of γ, α, and ζ are plotted on the same figures.

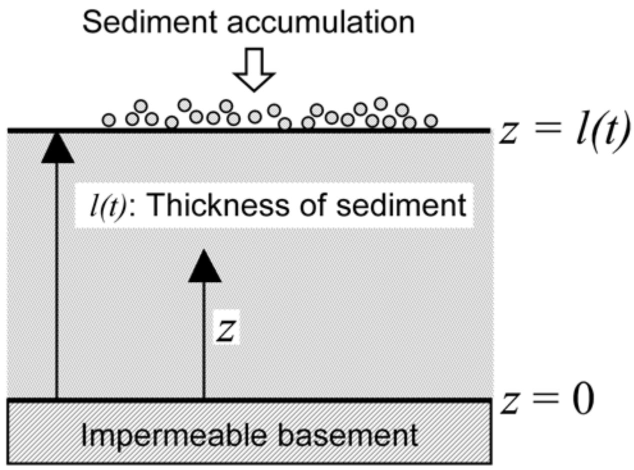

Figure 7. One-dimensional sedimentation model for the prediction of overpressure. Fluid flows only vertically, and sediments accumulate on the rising surface.

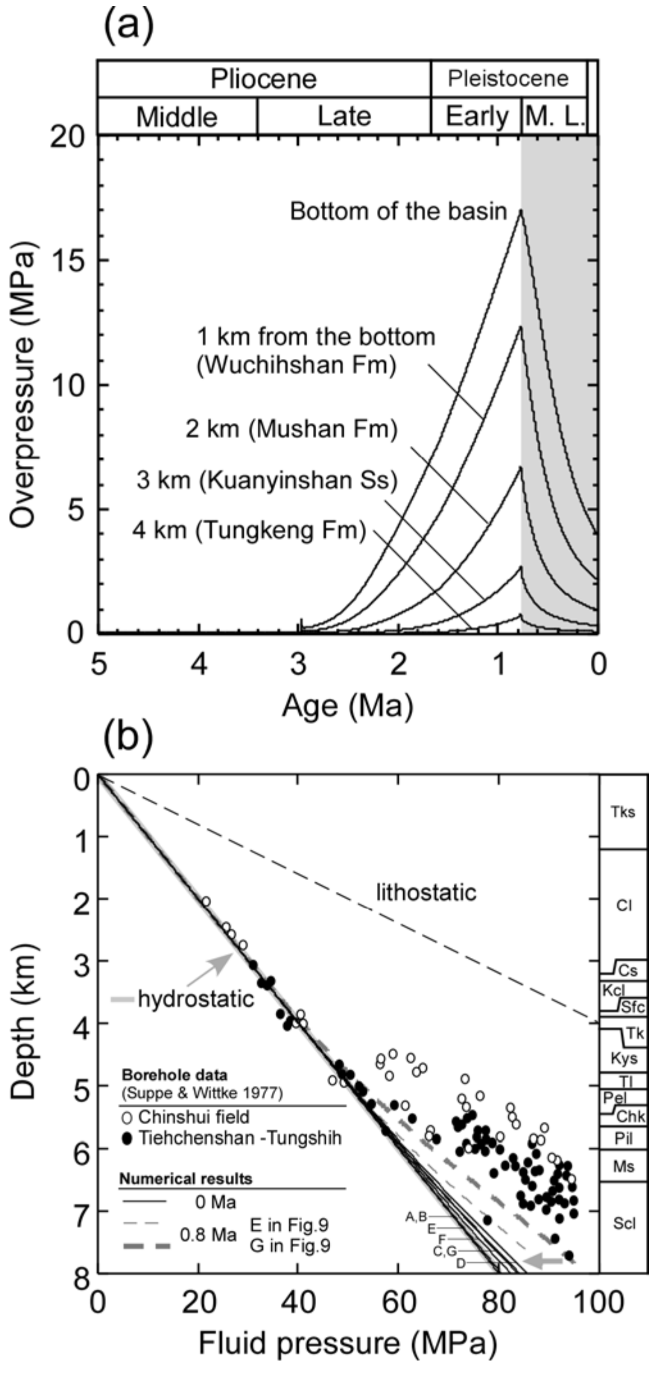

Figure 8. Numerical modeling results for (a) overpressure history and (b) fluid pressure distribution at present (0 Ma) and at 0.8 Ma in the Western Foothills in the case of no fluid influx at depth. Overpressure history is plotted for different horizons at various depths from the bottom of the basin,

using the parameter values of curve G (Fig. 9). Numerical calculations were performed for 30 to 0 Ma. Observed data shown in (b) are modified from Suppe and Wittke [1977]. The parameter values of curves A to G in (b) are given in Fig. 9. The solid lines are the simulated fluid pressure distributions at 0 Ma, and the dashed lines are at 0.8 Ma.

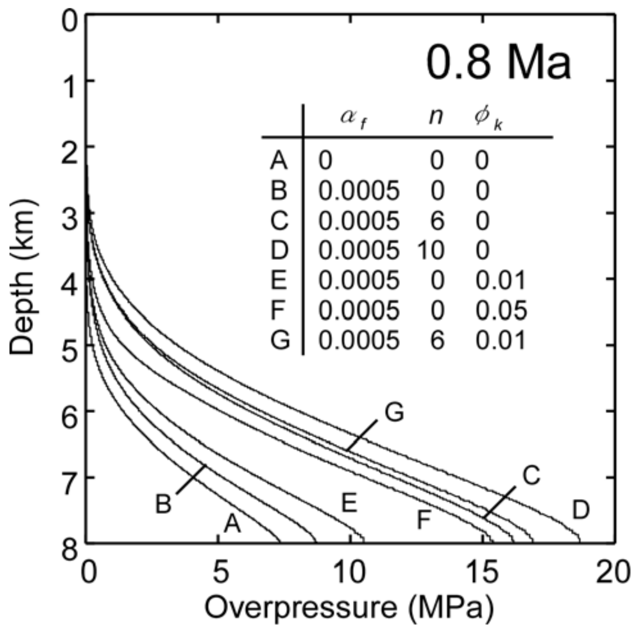

Figure 9. Predicted overpressure (excess fluid pressure above hydrostatic) distributions under various conditions at 0.8 Ma in the Western Foothills in the case of no fluid influx at depth. α_f, n, and Φ_k were changed to investigate the influence of thermal expansion of water, clay mineral dehydration, and hydrocarbon generation, respectively, on the excess fluid pressure generation.

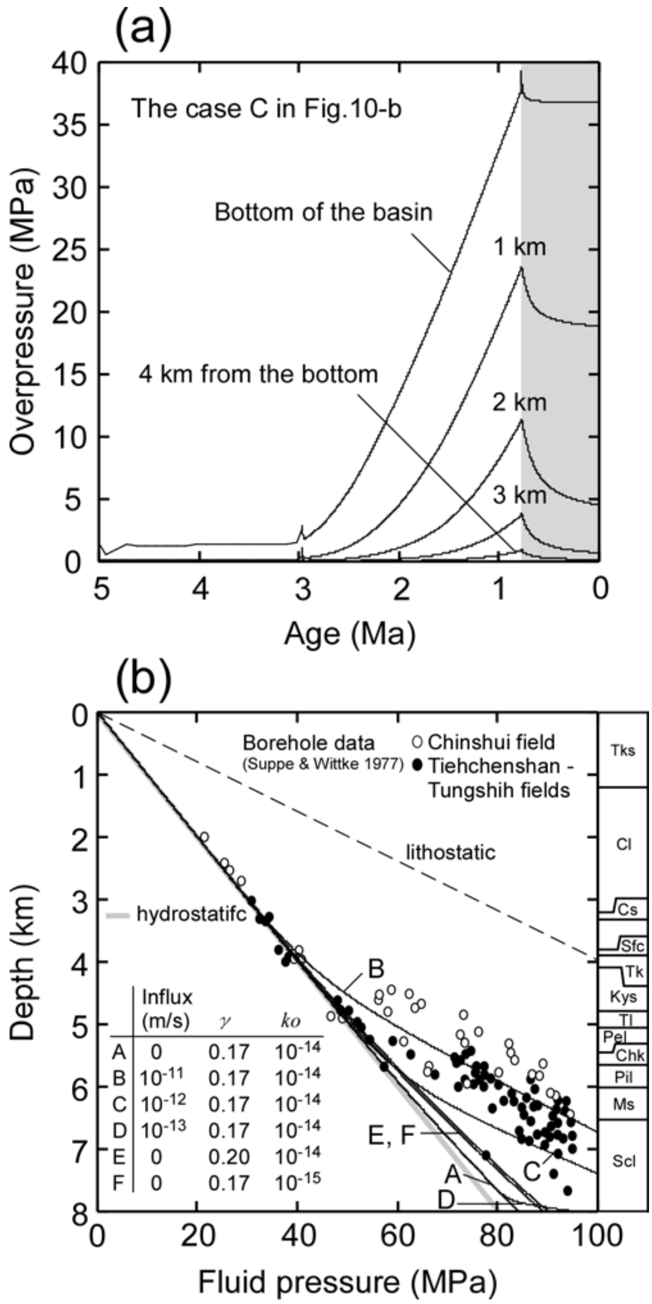

Figure 10. (a) Predicted overpressure evolution history at various depths for the parameter values of curve C (Fig. 10b). (b) The overpressure distribution in the Western Foothills was predicted by assuming a continuous fluid influx from the bottom of the basin (curves B–D) and by underestimating

permeability (curves A, E, and F). Curves B to D assume a constant fluid influx from the bottom of the basin throughout the entire geological period. The pressure sensitivity of permeability γ is changed in case E, and the initial permeability k_0 in case F.

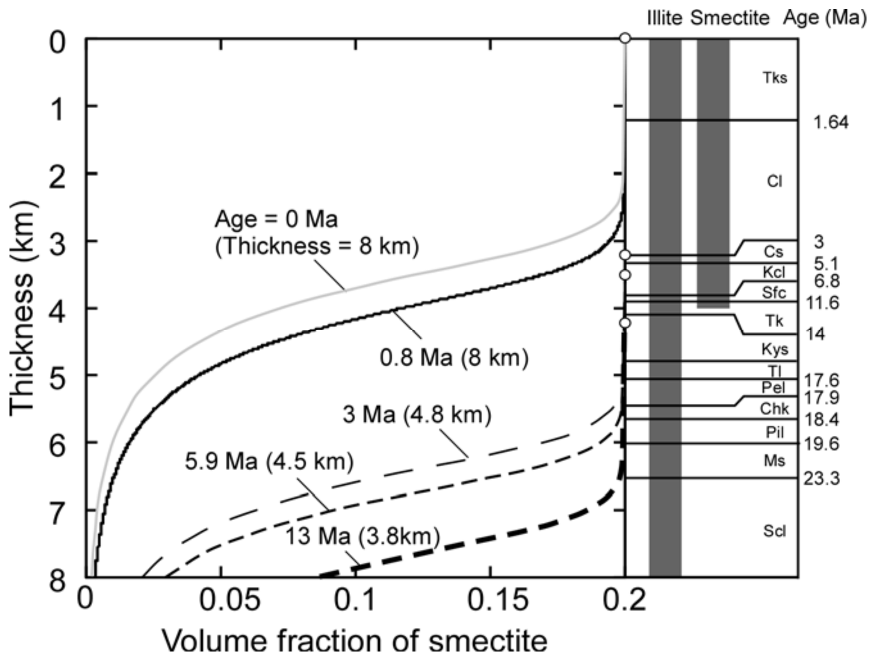

Figure 11. The volume fraction of smectite Φ_{sm} plotted against the accumulation thickness for various stratigraphic ages and the corresponding basin formations. The initial volume fraction of smectite is 0.2. The kinetic parameters used for the calculation are given in Table 2. The column on the right shows the distribution of illite and smectite as evaluated by X-ray diffraction analysis of oriented glycolated specimens. The curves are based

on a bottom depth of 8 km in this figure.

Period		Group / Formation		Thickness (m)	TOC	Overpressure	Oil production	Sediment composition	Tectonic events
Pleistocene	Late	Terrace deposits		2 - 5					Rapid deformation
	Early	Toukoshan (Tks)		1000 -1500				Orogenic sediment	Infill of orogenic sediments
Pliocene	Late	Cholan (Cl)		2000					
	Early	Chinshui Sh. (Cs)		80 -100					High-intensity collision (3 Ma)
		Kueichulin (Kcl)	Yutengping Ss.	271 - 660					Slight collision (5 Ma)
			Shiliufen Ss.	20 - 40					
Miocene	Late		Kuantaoshan Ss.	150 - 280					
	Middle	Shangfuchi Ss. (Sfc)		60 - 150	0.51				Initial collision of the arc - continent collision (12 Ma)
		Tungkeng (Tk)		550 - 750	0.94			Continental derived sediment	
		Kuanyinshan Ss. (Kys)		330 - 450	0.6				
	Early	Talu Sh. (Tl)		250 - 340	0.17-1.56				
		Peiliao Ss. (Pei)		300 - 400	0.17-0.5				
		Chuhuangkeng (Chk)		220	0.47-0.96				
		Piling Sh. (Pil)		450 - 500	0.58-0.61				
		Mushan (Ms)		450 - 700	0.34-1.89				
Oligocene		Shuichangliu (Scl)		900 -1200					

Table 1. Tectonostratigraphic, hydrological, and geochemical information for the north-central Western Foothills of Taiwan. The stratigraphic column is compiled from the Tungshih section [Suppe and Wittke, 1977; Lee, 2000]. TOC was evaluated at the Tiehchenshan field, and data are modified from Chiu and Chou [1991].

Symbol	Value	Units	Comment and Reference
α_f	5×10^{-4}	$^{o}C^{-1}$	Coefficient of thermal expansibility of fluid (Luo & Vasseur 1992)
β_f	4.4×10^{-10}	Pa^{-1}	Compressibility of fluid (Luo & Vasseur 1992)
ρ_s	2500	kgm^{-3}	Bulk density of sediments
ρ_w	1000	kgm^{-3}	Bulk density of water
Φ_0	0.6		Initial porosity
k_0	10^{-14}	m^2	Initial permeability
$\partial T/\partial z$	30	$^{o}Ckm^{-1}$	Geothermal gradient (Suppe & Wittke 1977)
Asm	5.2×10^{7}	s^{-1}	Pre-exponential constant of smectite transition (Pytte & Reynolds 1988)
Esm	138	$KJmol^{-1}$	Activation energy of smectite transition (Pytte & Reynolds 1988)
n	2 - 10		Number of moles water in the dehydration reaction (Freed & Peacor 1989)
V_f/V_{sm}	0.056		Molar volume of water per molar volume of smectite (Wangen 2001)
Φ_{sm}	0.2		Initial volume fraction of smectite (Wangen 2001)
A_k	2×10^{12}	s^{-1}	Pre-exponential constant of kerogen transition (Chiu et al., 1996)
E_k	200-300	$KJmol^{-1}$	Activation energy of kerogen transition (Chiu et al, 1996)
Φ_k	0.001-0.05		Initial volume fraction of kerogen (Chiu et al, 1996)
α	0.0006	MPa^{-1}	Compaction coefficient (Experimental determination)
γ	0.17	MPa^{-1}	Permeabiltiy sensitivity (Experimental determination)
ξ	0.003	MPa^{-1}	Skempton's coefficient sensitivity (Experimental determination)
ρ_k/ρ_0	1.25		Volume expansion factor: kerogen to oil (Wangen 2001)

Table 2. Physical and kinetic parameters used in the numerical model.